Plasmonic Nanoparticles and Island Films for Solar Energy Harvesting: A Comparative Study of Cu, Al, Ag and Au Performance

Ivana Fabijanić [1], Vesna Janicki [1], Josep Ferré-Borrull [2] , Matej Bubaš [1], Vesna Blažek Bregović [1], Lluis F. Marsal [2] and Jordi Sancho-Parramon [1,*]

[1] Ruđer Bošković Institute, Bijenička cesta 54, 10000 Zagreb, Croatia; ifabijan@irb.hr (I.F.); janicki@irb.hr (V.J.); Matej.Bubas@irb.hr (M.B.); Vesna.Blazek.Bregovic@irb.hr (V.B.B.)
[2] Department of Electronic, Electrical and Automatic Engineering, Universitat Rovira i Virgili, Avinguda dels Països Catalans, 26, 43007 Tarragona, Spain; josep.ferre@urv.cat (J.F.-B.); lluis.marsal@urv.cat (L.F.M.)
* Correspondence: jsancho@irb.hr

check for
updates

Abstract: Alternative materials that can potentially replace Au and Ag in plasmonics and broaden its application potential have been actively investigated over the last decade. Cu and Al have been usually overlooked as plasmonic material candidates because they are prone to oxidisation. In this work the plasmonic performance of Cu and Al is investigated using numerical simulations of different nanostructures (spheres, cubes, rods and particle dimers) and taking into account the presence of oxidisation. It is shown that geometry can play a dominant role over material properties and the performance of Cu and Al becomes comparable to that of Ag and Au for systems of non-spherical particles and strong electromagnetic coupling among particles. This observation is experimentally confirmed by the fabrication and characterisation of Cu and Al metal island films. Optical characterisation of the samples reveals a comparable performance of these metals to that obtained for Ag and Au and suggests that Cu and Al metal island films can offer an efficient low-cost platform for solar energy harvesting, as shown in water vapour generation proof of concept experiments.

1. Introduction

Localised surface plasmons are collective electron oscillations taking place at the interface between a metal nanoparticle and its surroundings and can be easily excited by optical radiation. Sub-wavelength localisation, electromagnetic field enhancement, large absorption and extinction cross sections and sensitivity to environment modifications have enabled the design of multiple novel applications and the establishment of plasmonics as a promising research area for future technologies [1–3]. Optimal performance of most plasmonic applications imposes negative real part of the dielectric function and negligible losses as the basic criteria for material selection. Therefore, Ag has been the primary choice for many applications. However, its chemical reactivity limits device life-time and thus Au is often preferred over Ag. In any case, Ag and Au possess some disadvantages such as scarcity, price, increased losses due to interband transitions and difficulty to tune the plasmon resonance beyond the visible range. Many types of materials that might alleviate one or more of these limitations have been investigated over the last decade. Thus, nitrides, oxides, silicides, doped semiconductors

and 2D materials have been proposed as plasmonic alternative materials with better performance than Ag and Au depending on the application and its operational spectral range [4,5].

Other metals with dielectric function governed by a Drude-like response in the optical range have been also considered as alternatives to Ag and Au [6]. Among them, Cu is a potential candidate with performance possibly comparable to Ag and Au [7] but with a strong tendency to oxidise [8] that can dramatically reduce the plasmonic response of nanoparticles [9]. However, oxidisation can be prevented by ultra-thin coatings of different materials [9,10] or treating the nanoparticles with corrosion inhibitors [11]. In addition, partial oxidisation can have a mild effect in the plasmonic resonance for certain Cu nanostructure morphologies [12] and it can even result in an increase of field enhancement and extinction cross sections [13]. Another potential candidate is Al, that shows plasmonic response in the ultraviolet range due to its high plasma frequency [14]. Yet, Al plasmon resonances can be tuned into the visible range by modification of particle shape [15,16]. Al oxidisation is typically limited to a very thin (≈ 2 nm) passivation Al_2O_3 overlayer that is stable over months [17] and results in a moderate quenching and red-shift of the plasmon resonance [16]. Al presents strong interband transition around 1.5 eV [6] that can significantly damp the plasmonic resonance in the visible and near-infrared region but also give place to hybrid modes in the scattering spectra [14]. Despite the mentioned drawbacks, Cu and Al are several orders of magnitude more available and cheaper than Ag and, especially, Au. Therefore, there is a growing interest in these materials as major candidates for future low-cost and large-scale deployment of plasmonic applications.

In the present work we numerically investigate the plasmon resonances of Ag, Au, Cu and Al for different nanoparticle geometries, including spheres, cubes, rods and particle dimers. It appears that in the small particle limit Ag and Au are significantly better for plasmonics than Al and Cu. However, non-spherical morphology, radiation damping and electromagnetic coupling bring the performance of all these materials to a similar level. In order to verify these conclusions, metal island films, i.e., nearly two-dimensional nanoparticle systems with broad size and shape distribution, are fabricated using electron beam evaporation. Optical characterisation confirms a comparable effective optical response for all the materials. Finally, Au and Cu metal island films are deposited on nanoporous Al_2O_3 and used for water vapour generation experiments, as an example of solar energy harvesting application. Overall, the large availability of these materials and the well-established used fabrication techniques make Cu and Al metal island films structures with large potential for widespread use of plasmonic-based devices.

2. Plasmonic Response of Ag, Au, Cu and Al Nanoparticles

Figure 1 shows the dielectric function frequency dependence for Au, Ag, Cu and Al taken from literature [6,18]. The real part shows larger negative values for Al than for Ag, Cu and Au, since it has three free electrons per atom instead of one as the others and therefore presents a larger plasma frequency. The imaginary part reveals interband transitions in ultraviolet (Ag), ultraviolet-visible (Cu and Au) and infrared (Al) part of spectra. Below the interband transitions region, Cu presents slightly larger losses than Au.
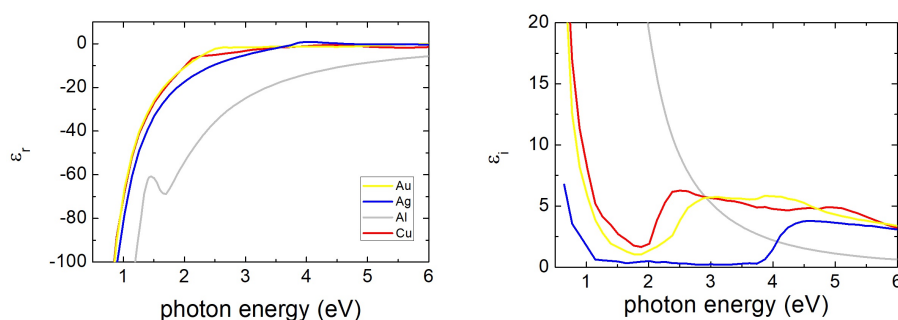

Figure 1. Real (left) and imaginary (right) parts of the dielectric function of Ag, Au, Cu (Reference [18]) and Al (Reference [6]) as function of photon energy.

In the present study we use tabulated bulk optical constants taken from literature (Figure 1) for numerical simulations, i.e., we only consider extrinsic size effects on the surface plasmon resonance. In case of particles with sizes below the free electron mean path, confinement effects result in enhanced losses in the Drude term and plasmon broadening [19] while for particles in the size range of very few nanometres quantum effects play a dominant role and blue shift the resonances [20].

2.1. Spherical Particles: Small Particle Limit and Size Effects

In the case of spherical particles much smaller than the wavelength of the interacting radiation, the electromagnetic response of nanoparticles can be approximated to the one of a point-dipole and is completely determined by the static polarizability [21]:

$$\alpha = 4\pi\epsilon_0 a^3 \frac{\epsilon_p - \epsilon_h}{\epsilon_p + 2\epsilon_h}, \tag{1}$$

where ϵ_p and ϵ_h are the particle and the host matrix dielectric function respectively, ϵ_0 is the vacuum permittivity and a is the particle radius. Figure 2 shows the absolute values of the polarizabilities for different metals as a function of the photon energy and host dielectric function. The polarizability achieves large values when $\epsilon_p \approx -2\epsilon_h$, corresponding to the plasmon resonance excitation. For purely dielectric host (real ϵ_h) the only limiting factor on the magnitude of the polarizability is the imaginary part of ϵ_p, that prevents the denominator to vanish. Therefore, in agreement with the data shown in Figure 1, Ag presents by far the strongest plasmonic response. Cu and Au show comparable characteristics, although Au has a better performance due to its smaller losses. Increasing ϵ_h results in red-shift of the plasmon resonance, that moves away from the interband transition region in Au and Cu and improves materials performance. However, in the case of Al the red-shift brings the resonance close to the interband transition centred around 1.5 eV and the plasmon resonance becomes damped.
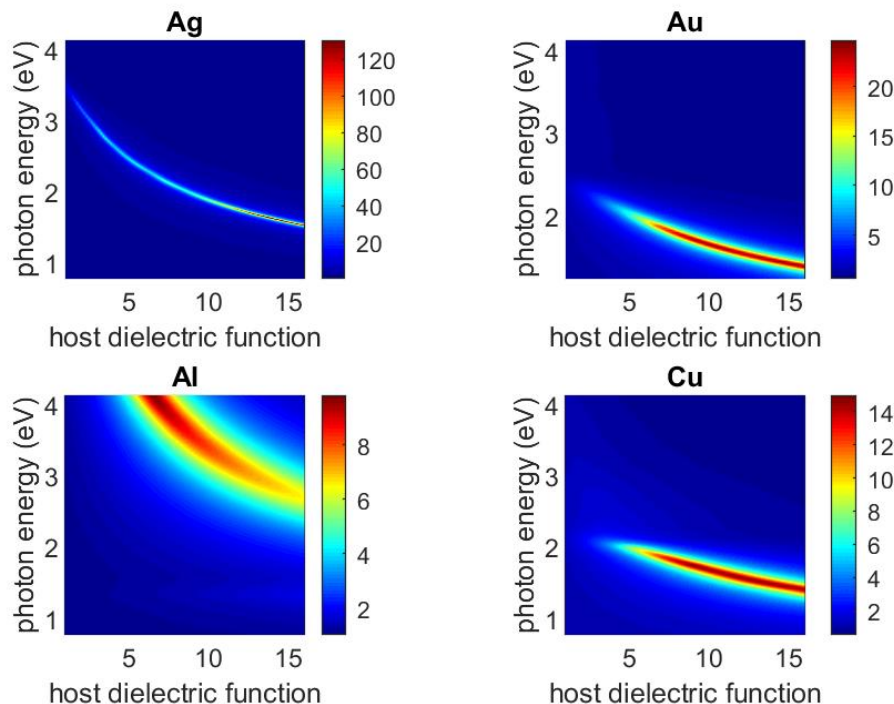

Figure 2. Absolute value of normalized polarizability ($\alpha / \left(4\pi\epsilon_0 a^3\right)$, Equation (1) for Ag, Au, Al and Cu single particles in the electrostatic dipole limit as function of photon energy and ϵ_h.

If the particle dimensions are comparable to the wavelength of light, retardation effects start to play a significant role and additional quenching mechanisms, such as radiation damping, become significant.

In the first approximation, the static polarizability (Equation (1)) should be replaced by its dynamic counterpart, α_d:

$$\alpha_d = \frac{\alpha}{1 - \frac{2}{3}ik^3\alpha}, \tag{2}$$

where k is the wavenumber and i the imaginary unit. Expression (2) shows that, in addition to losses, particle size can be an extrinsic limiting factor on the plasmonic response. Extinction efficiencies for particles of different materials with radius $a = 100$ nm and embedded in a water-like environment ($\epsilon_h = 1.77$) have been calculated using Mie theory (Figure 3). The dipolar resonance, centred around 750 nm, is much broader than in the small particle limit due to the mentioned additional damping mechanisms. In addition, it presents very similar characteristics regardless the considered material. This observation can be intuitively understood by the fact that geometrical optics becomes an increasingly valid framework for the electromagnetic response of particles when their size becomes larger. In this limit all these metals behave as nearly perfect reflectors of radiation regardless of their shape and the main difference can be found in their colour, determined by the onset of interband transitions. Simulated data reveals the appearance of additional resonances in the short wavelength region, corresponding to the excitation of multipolar plasmon modes.
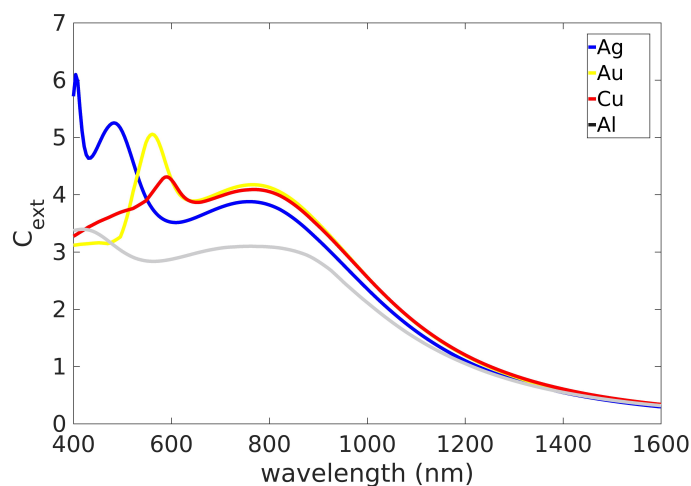

Figure 3. Extinction efficiency for Ag, Au, Al and Cu particles with radius $a = 100$ nm embedded in water ($\epsilon_h = 1.77$) calculated according Mie theory.

2.2. Shape Effects

In order to analyse the role of shape on the plasmonic resonances of different materials, two systems are considered: (i) the transition from a sphere to a cube and (ii) the transition from a sphere to a rod. The first case primarily reveals the effects of roundness/sharpness while in the second case the influence of aspect ratio is evidenced. Numerical calculations are done in the context of the boundary element method that can tackle arbitrarily shaped particles (Section 5.1).

Let us assume a nanocube of side length $L = 50$ nm in which the edges and corners are progressively rounded until it becomes a nano-sphere with radius $a = 25$ nm. The roundness degree, S, of such a semi-cube is defined as the ratio between twice the rounding radius and the cube length ($S = 2a/L$). Thus, $S = 0$ corresponds to a cube and $S = 1$ represents a sphere. Simulations of the extinction cross section for such systems in a water environment are shown in Figure 4. In all the cases, the surface plasmon resonance red-shifts as the particle transforms from a sphere into a cube. This shift is accompanied by resonance narrowing, especially for Au, Cu and Al. This observation is in contrast to the size increase case discussed before and enables shape-controlled resonance tuning without additional damping. For all materials, the extinction spectra of a sphere is dominated by the dipolar resonance. Red-shift of this mode and additional resonances take place when the particle

sharpness increases. These resonances arise from high order multipolar modes of a sphere that evolve into red-shifted corner modes for a cube, with charge essentially located at the cube vertices [22]. These resonances merge into a single peak in Cu and Au, but they can be well resolved for Ag and Al thanks to the lack of interband transitions in the spectral range where the resonances take place. Cu nanocubes have a narrower extinction line-shape than Au ones, in agreement with recent experimental studies [23]. This fact is connected to the quenching of high order corner modes that overlap with the lowest energy resonance. In comparison to Au, the wider range of Cu interband transitions damps more effectively these high order modes and the overall line-shape is narrower. Shaping Al spheres into cubes brings the resonances into the visible range while keeping a moderate size, i.e., with no significant quenching and broadening. Overall, it appears that improvement of plasmonic performance by shape control is more relevant for Al and Cu than for Au and, especially, Ag. The role of size in nanocubes is similar to the case of spheres discussed in the previous section. Figure 5 shows the extinction efficiency for small ($L = 20$ nm) and large ($L = 200$ nm) cubes. For small particles, the reduced losses in Ag enable excitation of several narrow and intense corner modes, while Au and Cu show much weaker resonances that appear only beyond the interband transitions region. In the case of large particles, retardation makes the response of different materials similar.
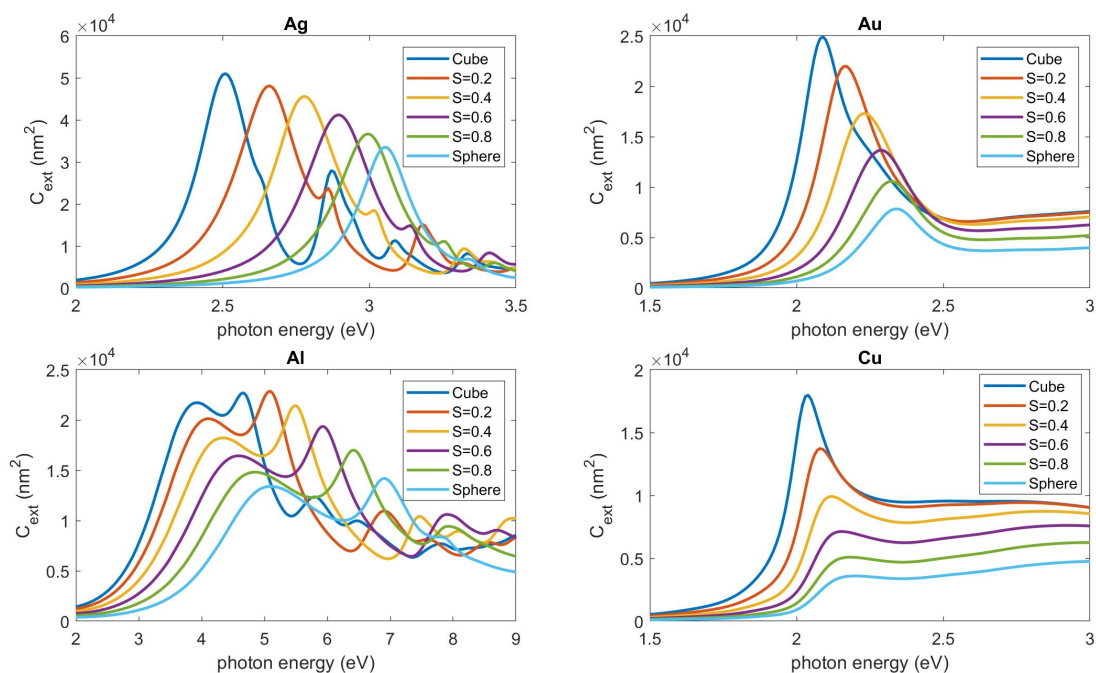

Figure 4. Extinction efficiency for Ag, Au, Al and Cu semi-cubes with varying shape parameter (S) and constant length of ($L = 25$ nm) embedded in water ($\epsilon_h = 1.77$).
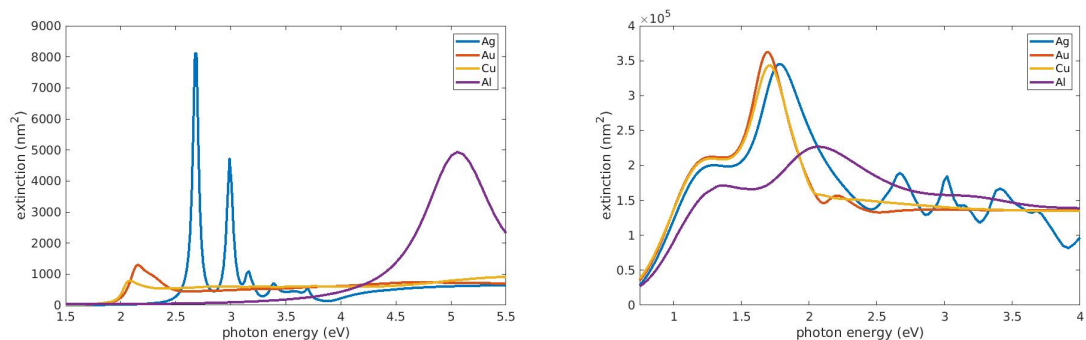

Figure 5. Extinction efficiency for Ag, Au, Al and Cu nanocube with side length $L = 20$ (left) and 200 (right) nm embedded in water ($\epsilon_h = 1.77$).

The effect of nanoparticle aspect ratio change on its plasmonic response has been previously studied in detail [19,24]. Particularly, it has been shown that increasing the aspect ratio can improve its plasmonic response as the resonance might be less affected by losses [25]. In order to compare the relative improvement in performance for different materials we consider here a sphere to nanorod transition. Nanorods are modelled as cylinders of total length L and diameter $2a$, terminated by two hemispherical caps with diameter $2a$. The aspect ratio AR is then defined as the ratio between the total rod length and its diameter ($AR = L/2a$), with the limiting case $AR = 1$ representing a sphere. A plane wave polarized in the direction of the nanorod long axis is taken as illumination. It has been reported that the dipolar plasmon resonance red-shifts and new modes appear in the spectra as the nanorod aspect ratio increases [26,27]. Since a nanorod can be roughly approximated as a one-dimensional structure, these higher order modes are often associated to Fabry-Perot oscillations within the total length of the rod [28,29]. Extinction cross sections for nanorods made of the investigated materials are shown in Figure 6 and qualitatively follow the reported behaviour. High multipolar modes are quenched in Au and Cu due to interband transitions. In the case of Al, when the dipolar resonance takes place close to 1.5 eV, the extinction line-shape is modified by the presence of interband transitions. Red-shift of the dipolar mode is accompanied by plasmon resonance strengthening and narrowing. In the limit of very large AR, the resonances of all materials become comparable. Indeed, as the nanorod becomes larger its response can be well approximated to the one of an ideal half-wave antenna. In this case the resonance condition is determined by the nanorod length and not by the specific material properties [30]. Since the response of all materials becomes comparable, the largest improvement of the plasmonic response due to AR increase takes place for Cu and Al. In the case of Al, one should note the large tuning degree of the resonance energy when the aspect ratio goes from 1 to 4, shifting nearly 4 eV, i.e., more than twice the shift observed for Ag, Au and Cu.
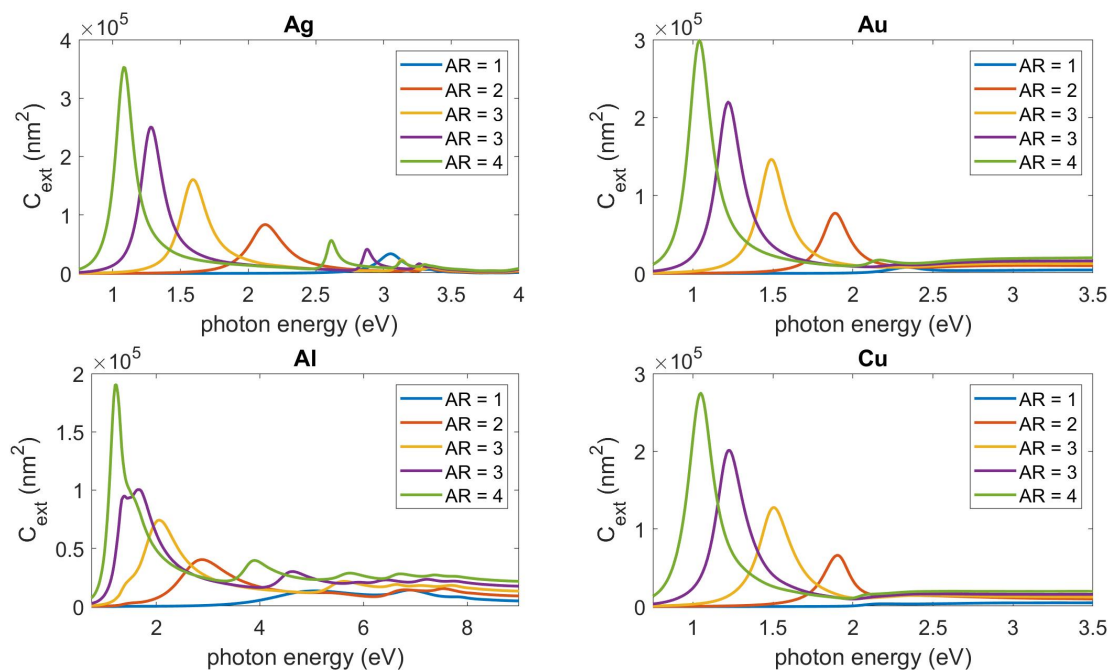

Figure 6. Extinction efficiency for Ag, Au, Al and Cu nanorods with varying aspect ratio (AR) and constant hemispherical cap radius (a = 25 nm) embedded in water (ϵ_h = 1.77).

2.3. Plasmon Hybridisation: Dimers

In order to study the influence of electromagnetic coupling among particles, the generalized multiple particle Mie theory described in Section 5.1 is used to simulate the response of two spherical particles separated by a small distance and excited by a plane wave polarized parallel to the axis defined by the particles. This dimer configuration leads to a large electromagnetic field enhancement

at the region located between particles and increased extinction cross section as result of in-phase hybridisation of the plasmonic mode of individual particles [31]. Figure 7 shows the scattering efficiency for two closely located particles as a function of the separation distance. For large separation distances, electromagnetic interaction is weak and the dimer behaviour is essentially defined by the individual particle response. As the particles approach to each other, coupling increases and the hybrid modes significantly depart from the single particle modes. Qualitatively, similar trends are observed for dimers of other particle shapes such as cubes [32] or rods [26]. For all materials the plasmonic resonance of the coupled system red-shifts and increases in strength when the particle separation reduces, with the largest relative changes taking place for Cu. Figure 8 shows the electromagnetic field distribution at the hot-spot region. It can be noted that Cu outperforms Au regarding maximum field enhancement.
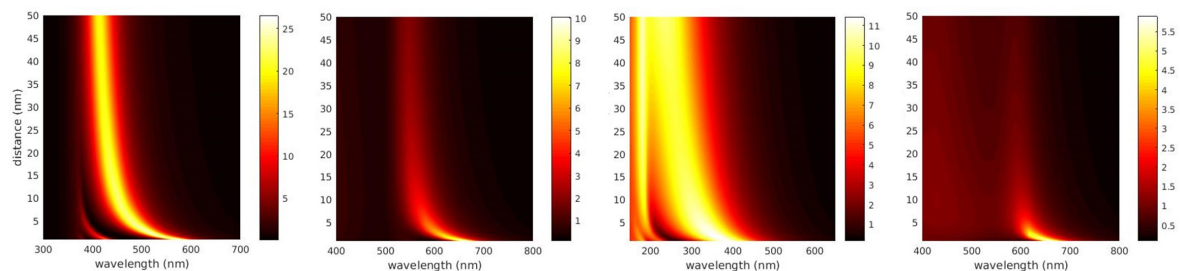
Figure 7. Scattering efficiency for Ag, Au, Al and Cu dimers (left to right) with radius $a = 25$ nm embedded in water and varying particle separation. Excitation polarisation is parallel to the dimer axis.
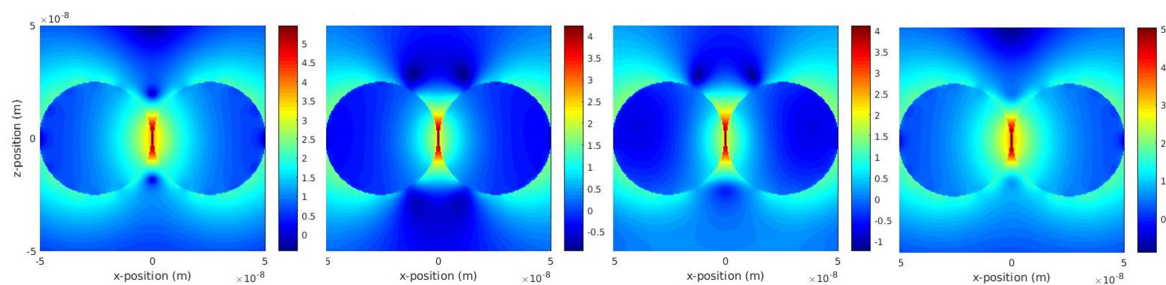
Figure 8. Electric field intensity enhancement (logarithmic scale) for Ag, Au, Al and Cu dimers (left to right) with radius $a = 25$ nm embedded in water and interparticle separation of 1 nm. Excitation polarisation is parallel to the dimer axis and the near field map corresponds to the plane defined by the polarisation and propagation directions. Calculations are done at the resonance photon energy.

2.4. Effect of Oxidisation

The effect of superficial oxidisation in the plasmonic response of Cu single particle and dimers is investigated using the extension of Mie theory for coated particles (See Section 5.1). Optical constants of Cu_2O for shell are taken from literature [6]. Figure 9 shows the average field enhancement of a particle with radius $a = 25$ nm as function of the oxide shell thickness. Increasing the Cu_2O shell red-shifts the resonance, alleviates the effect of interband transitions and can substantially increase the average enhancement (over 50% for a 5 nm oxide overlayer). This result is in agreement with previous numerical simulations [13] that pointed out the counter-intuitive beneficial effects of oxidisation. Stronger oxidisation further red-shifts the resonance but leads into too large screening of the field enhancement at the particle surface and the net effect is lesser than in unoxidised Cu particle.

The situation for a dimer is different since field enhancement is essentially placed at the hot-spot generated between particles as a result of strong charge localisation at the closest surface regions of the particles. Thus, the presence of a very thin oxide layer effectively increases the distance between charges of both particles, reduces electromagnetic coupling and quickly quenches the field enhancement. As shown in Figure 9 a 2 nm thick Cu_2O shell suffices to reduce the average field enhancement to half

of the values corresponding to an unoxidised Cu dimer. The results for Al/Al$_2$O$_3$ core-shell particles and dimers are qualitatively similar to those here discussed for the Cu/Cu$_2$O system.

Although the initial stages of Cu oxidisation are typically characterised by the formation of a Cu$_2$O overlayer, partial formation of CuO has also been observed [8]. We have calculated the plasmonic performance of single particles and dimers for Cu/CuO core-shell particle and obtained a response close to the reported for Cu/Cu$_2$O particles. The reason is that CuO and Cu$_2$O present a similar refractive index in the wavelength range where Cu plasmon resonance takes place.
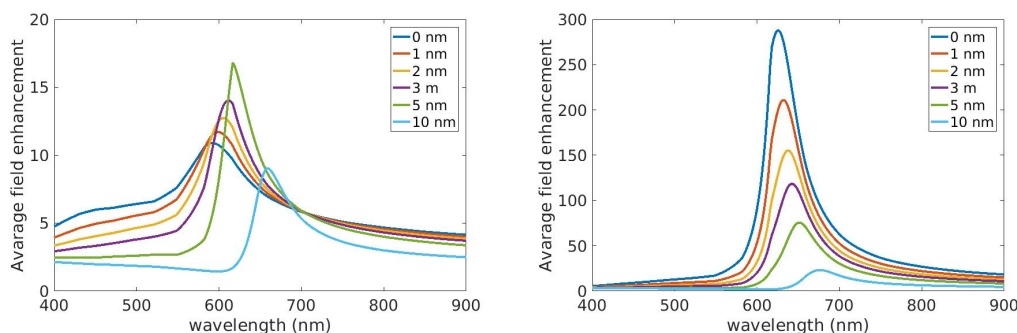

Figure 9. Average field enhancement over Cu particle surface with radius *a* = 25 nm in water assuming different Cu$_2$O shell thickness. Left: single particle. Right: particle dimer separated by 2 nm and excited by a plane wave polarized in the dimer axis direction. Note the different ranges for the average field enhancement axis.

3. Metal Island Films for Solar Energy Harvesting

The numerical investigations presented in the previous section indicate that control of size, shape and degree of interaction among particles can bring the plasmonic properties of Cu and Al structures close to those of Ag and Au. Particularly, it appears that highly disordered systems like metal island films, i.e., with relatively large size and shape distributions and randomly located particles, can provide a suitable framework to obtain a comparable performance for all these materials.

3.1. Fabrication and Characterisation of Metal Island Films

Metal island films of different materials were deposited using electron beam evaporation in a modified Varian chamber (see Section 5.2). Previous research on Ag, Au and Cu island films fabricated in this way [12,33,34] indicates that a small amount of deposited metal (mass thickness, d_m, in the range 1 to 2 nm) results in well-isolated clusters with nearly spherical shape, closely resembling the morphology described in Section 2.1. Increasing the amount of deposited metal results in larger non-spherical particles with broad size and shape distribution and reduced interparticle distance [35,36]. In such situation Cu and Al island films might present a comparable performance to standard plasmonic materials. However, if d_m is too large and approaches the percolation threshold (typically between a few and a few tens of nanometres depending on the material, substrate and its temperature during deposition), islands aggregation takes place and the film behaviour becomes close to that of bulk material [37,38]. Taking into account these observations, a value of d_m = 5 nm was chosen for deposition of all materials.

The optical response of a metal island film in the just depicted regime can be accurately described using a multiple oscillator model to represent the effective dielectric function ϵ_{eff}. Thus, the following dispersion model was used:

$$\epsilon_{eff}(E) = \epsilon_\infty + \sum_{k=1}^{n} \left[\epsilon_{GR,k}(E) + i\epsilon_{GI,k}(E) \right] \tag{3}$$

with

$$\epsilon_{GI,k}\left(E\right) = A_k \left[\exp^{-\left(\frac{E-E_k}{B_k}\right)^2} - \exp^{-\left(\frac{E+E_k}{B_k}\right)^2} \right] \tag{4}$$

$$\epsilon_{GR,k}\left(E\right) = \frac{2}{\pi} P \int_0^\infty \frac{\xi \epsilon_{GI,k}\left(\xi\right)}{\xi^2 - E^2} d\xi \tag{5}$$

where E is the photon energy. The first term on the right-hand side of Equation (3), ϵ_∞, is the contribution of polarisation mechanisms that occur at photon energies above the spectral range of interest. The second term is a sum of Gaussian oscillators that can be used to model localised surface plasmon resonance and interband transitions. It appears that this type of oscillators is more appropriate than the classical Lorentz model in case of complex systems like metal island films, in which the size and shape distribution of particles often results into a nearly Gaussian distribution of resonances [34,38]. Each Gaussian oscillator is defined through its amplitude (A_k), central energy (E_k) and broadening (B_k). Usually, one to two oscillators are necessary to describe the plasmonic resonances and one additional oscillator is required for each interband transition appearing in the measured spectral range.

The resulting effective dielectric function for the fabricated Ag, Au, Cu and Al island films is shown in Figure 10. It can be noticed that the peak values of the imaginary part of the dielectric function are very similar in all cases, as expected from plasmon resonances of comparable strength. They take place at different photon energies, which is also in agreement with the previous simulations. The red-shift of Cu plasmon resonance in comparison with Au can be explained in terms of Cu oxidisation. Indeed, measurements of aged samples show a progressive red-shift of Cu island films [12]. Al presents a significantly wider plasmon resonance than the other materials, that can be explained by the good wetting characteristics of Al on dielectric surfaces. In this case, the resulting islands morphology can be expected to be close to a percolated film [39], as confirmed by the effective thickness values inferred from ellipsometry (12, 11, 10.5 and 7 nm for Ag, Au, Cu and Al island films) that evidence the larger compacity of Al films compared to the other materials. Overall, the experimental results support the conclusion deduced from numerical simulations stating that in case of a highly disordered system the performance of different materials becomes comparable. Calculation of the effective dielectric function of metal islands films using numerical approaches, although possible, is out of the scope of this work due to its high complexity, that requires taking into account a large number of effects: electromagnetic coupling among differently shaped particles [40], complex shape distributions [41], size effects [42] or the asymmetric dielectric environment of islands [36].
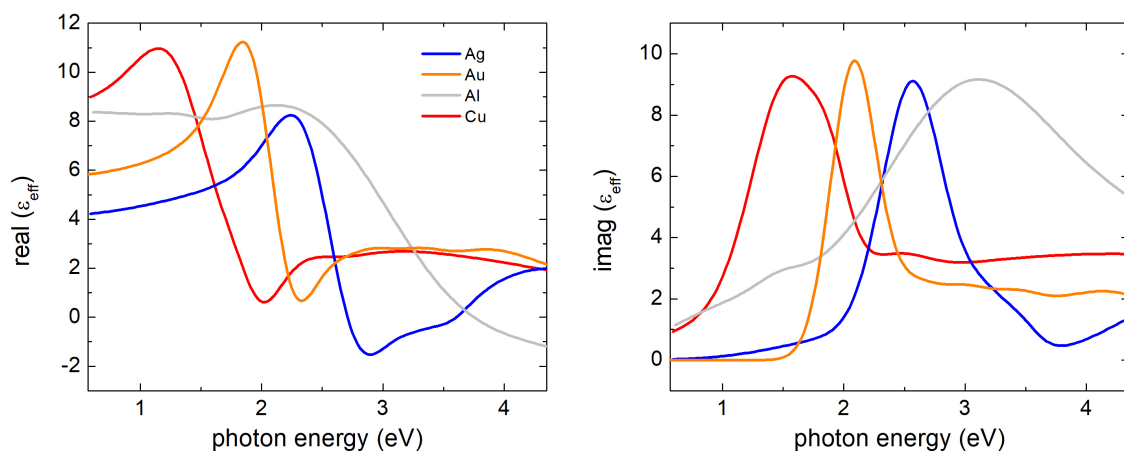

Figure 10. Real (left) and imaginary (right) of the effective dielectric function of fabricated metal island films of 5 nm mass thickness made of Ag, Au, Al and Cu as determined from ellipsometry measurements.

3.2. Metal Island Films in Porous Al₂O₃ Templates for Water Vapour Generation

Once verified that Cu and Al island films can present a similar plasmonic response to those made of Ag and of Au, we aim to test their potential in solar energy harvesting experiments. Cu and Al islands films can be attractive structures for low-cost and mass-production of plasmonic devices as they combine the advantage of using inexpensive and highly available materials with well-established fabrication techniques. As proof of concept study for solar energy harvesting, we investigate the generation of water vapour using Au and Cu island films. Excitation of plasmon resonance results in local heat transfer to the surrounding of metal nanoparticles, what has been shown to enable steam generation without bringing the bulk liquid to its boiling point [43]. It was shown that heat transfer of metal nanoparticles immersed in water is primarily directed to vaporisation by formation of nano-bubbles around the nanoparticles. In addition to isolated nanoparticles immersed in liquid other schemes have been used, such as porous membranes coated with randomly shaped and sized gold nanostructures [44,45]. It has been suggested that such structures can make a more effective use of solar energy irradiation spectrum as they possess broader absorption spectral characteristics in comparison with single particles.

Nanoporous alumina templates have been fabricated using a two-step anodisation process. Details on the fabrication and technical specification of the templates are described in Section 5.3. The templates were coated with Au or Cu particles using the same electron beam evaporation process used for deposition of metal island films on glass substrates. Samples were positioned right above the material source during deposition, enabling a deeper penetration of the evaporating materials in the alumina membrane and coating the interior walls of nanopores. Since Cu wets Al₂O₃ slightly better than Au, in order to have similar island morphology and interparticle distance among particles a smaller amount of Cu ($d_m = 8$ nm) than of Au ($d_m = 9$ nm) was deposited. The transmittance spectra of the Al₂O₃ templates before and after metal deposition are shown in Figure 11 (left), showing the dip around the plasmon resonance of Cu and Au and confirming the growth of isolated particles.

Scanning electron microscopy (SEM) pictures of the Au-coated nanoporous anodised alumina template is shown in Figure 11 (right). Due to the lower electronic density of Cu, electron microscopy images of Cu-coated template have limited resolution and the presence of particles cannot be discerned from SEM pictures. Yet, the existence of nanoparticles is confirmed from the transmittance spectra and the presence of Cu from energy dispersive spectroscopy. Au-coated templates, on the other hand, can be characterised by SEM with significantly larger resolution, confirming the presence of nanoparticles on the sample surface. The particles cover the interior walls of the pores as well, as evident from the SEM images taken with the sample tilted 35°. The tilted image clearly reveals the spiky structure of the sample surface, that helps reduce the overall reflectivity and enables larger interaction of light with the interior of the structure.
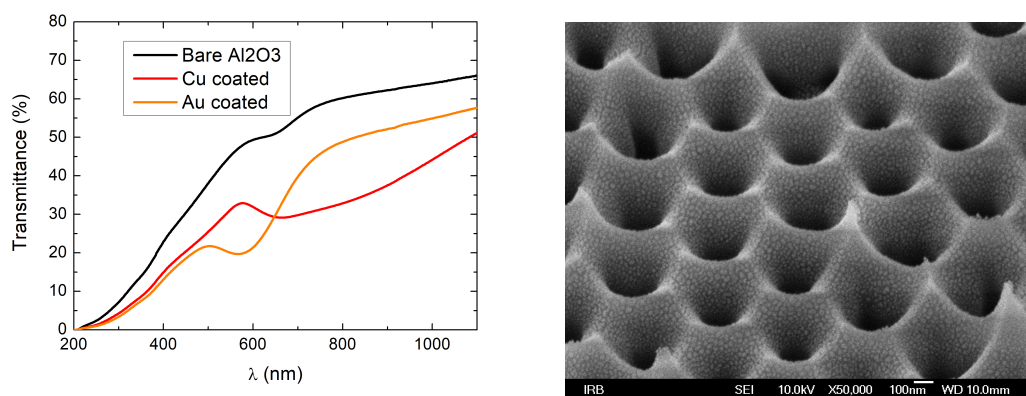

Figure 11. Left: Normal incidence transmittance of Al₂O₃ before and after the deposition of 9 nm mass thickness Au and 8 nm mass thickness Cu metal island films. Right: Scanning electron microscopy picture of the Au-coated Al₂O₃ template.

Coated templates were used for steam generation experiments (described in the Section 5.3) following the approach of other works [45]. The amount of generated steam was determined from measurements of the container-template-water system weight prior and after exposing the coated samples to solar illumination. Steam generation rate was 1.8 kg/m^2 per hour for Cu-coated template and 3.5 kg/m^2 per hour for Au-coated template. These values are well above the standard evaporation rate at normal laboratory conditions, verifying the potential of these structures for water vapour generation. The lower steam generation rate for Cu can be understood taking into account that the local temperature rise is primarily determined by absorption enhancement in nanoparticles [46]. As explained before (see Section 2.4) the plasmon resonance in strongly interacting particles is largely quenched upon Cu oxidisation, that appears to be unavoidable in steam generation experiments as the Cu-coated template is in direct contact with water. Therefore Au-coated templates, unaffected by oxidisation, can benefit from the generation of hot spots arising in closely located Au particles. In any case, taking into account the larger availability and lower cost of Cu in comparison with Au, Cu-based structures show strong potential for solar energy harvesting. Experiments repeated two weeks after the initial tests showed no significant steam generation rate variation for the Cu-coated template. Indeed, our previous findings indicate that oxidisation quickly takes place within few days after deposition and afterwards slowly progresses [12]. We plan to track the steam generation efficiency over a long time period and large number of experiments to evaluate the system life-time. In addition, optimisation of Cu island morphology and overcoating with ultrathin dielectric layers [9,10] in order to minimize the effect of oxidisation in these experiments is currently undergoing.

4. Conclusions

The plasmonic potential of Cu, Al, Ag and Au has been analysed using electrodynamic simulations of different types of standard nanoparticle systems, such as spheres, nanorods, nanocubes and dimers. It is shown that geometry can play a dominant role over material properties and the performance of Cu and Al can be comparable to that of Ag and Au for non-spherical particles and systems having strong electromagnetic interaction among particles.

This conclusion based on numerical simulations is experimentally confirmed by the fabrication and characterisation of Ag, Au, Cu and Al metal island films using a standard thin film technique (electron beam evaporation). Optical characterisation of the samples reveals a comparable performance of Cu and Al to that obtained for Ag and Au. Proof of concept experiments confirm that Cu-coated nanoporous alumina templates can be used for steam vapour generation with a lower efficiency, yet comparable, to Au-coated templates. Preventing oxidisation could further improve the performance of Cu-based structures and is a topic of current investigation.

Overall, taking into account the large availability of Cu and Al and the well-established island films fabrication techniques, structures based on these alternative materials offer a promising platform for low-cost plasmonic applications related to solar energy harvesting.

5. Materials and Methods

5.1. Numerical Methods

Calculation of the electromagnetic response of metal nanoparticles can be done analytically in the framework of Mie theory in case of a homogeneous spherical particle [21]. In short, the incident, scattered and internal electromagnetic fields are expanded in terms of vector spherical harmonics. The coefficients of the expansion are determined by imposing continuity conditions at the boundary between the metal nanoparticle and its environment. Typically, the number of terms to be considered in the expansion increases with particle size. Once the coefficients are determined, relevant electromagnetic parameters such as the scattering, extinction and absorption cross sections or the electromagnetic field enhancement, can be easily computed. In case of particles much smaller than

the wavelength of light, only the dipolar term remains in the multipolar expansion and all relevant properties can be straightforwardly calculated.

Mie theory can be expanded to consider other cases of interest, such as core-shell particles [21]. In this case internal fields in the core and shell regions, that can be determined using the additional boundary conditions at the core-shell interface, have to be taken into account as well. Finally, the extension of Mie theory to systems containing multiple particles [47] requires imposing that the field acting on each particle is the sum of the external field and the field scattered by the other particles. The resolution of the problem becomes more complex, as vector addition theorems are necessary in order to relate the fields expanded at different particles. Yet, the problem can be treated analytically and the method is faster and more precise than the more general purely numerical approaches.

For arbitrarily shaped nanoparticles, it is necessary to solve Maxwell equations using numerical approximations. During the last decades, a large number of methods have been developed, such as the dipole-dipole approximation, finite difference time domain methods, finite element method or the T-matrix method [48]. In the present work we have primarily used the boundary element method as developed by Garcia de Abajo [49]. In short, the arbitrary particle surface is discretized in small elements and then the effective surface charge and current densities are determined by imposing boundary conditions. Then the electromagnetic response of the system can be calculated from the surface densities. In the present work we have used the MNPBEM implementation of the boundary element method [50]. Optical constants of Ag, Cu and Au were taken from Ref. [18] and for Al, Ref. [6] was used.

5.2. Fabrication and Characterisation of Metal Island Films

Ag, Au, Cu and island films were deposited on silicon and BK7 glass substrates by electron beam evaporation using a modified Varian chamber. The base pressure was kept below 6×10^{-7} Torr. A quartz crystal was used to monitor the deposited mass thickness (d_m) that corresponds to the material density multiplied by the amount of deposited volume, i.e., the thickness of a fully compact film with the same mass as the deposited one. The deposition rate of metals was typically ≈ 1 Å/s. Substrates were pre-heated at 220 °C to enhance island growth. Prior to metal deposition both kind of substrates were pre-coated with a 80 nm thick SiO_2 layer in order to ensure the same conditions for island growth. Metal island films were left uncoated.

Transmittance measurements were taken in the range between 200 and 1100 nm using a Lambda 25 Perkin-Elmer spectrophotometer. Spectroscopic ellipsometry measurements were carried out in the spectral range between 0.57 and 4.6 eV and angles of incidence of 45°, 55° and 65° for glass substrates and 65°, 70° and 75° for silicon substrates with a J.A. Woollam V-VASE ellipsometer. Modelling of ellipsometric data using the WVASE software lead to retrieval of effective thicknesses and dielectric functions of the films. Scanning electron microscopy (SEM) plain view images were taken with a field-emission microscope Jeol JSM 7000F, typically working with an acceleration voltage of 15 kV.

5.3. Nanoporous Alumina Templates and Water Vapour Generation Experiments

A series of nanoporous alumina membranes were fabricated by aluminium anodisation [51,52] and used as templates for steam generation experiments. The total membrane thickness was ≈ 46 microns. The anodisation potential was set to 195 V and the electrolyte temperature was kept at -5 °C. Phosphoric acid was used for the electrolyte. Under these conditions, an interpore distance in the range of 300 nm was obtained. This interpore distance and the pore diameter (150 to 200 nm) were chosen from numerical simulations: large enough to enable metal nanoparticles to be efficiently deposited into the pores and small enough to avoid diffraction effects that could result in optical losses unrelated to absorption of metal island films.

Water vapour generation experiments were conducted focusing the spot of a solar simulator (SFA-300-A 300 W Small Collimated Beam Solar Simulator) down to 6.5 mm to fit onto the nanoporous Al_2O_3 template. The coated templates were placed in pyrex glass container filled with ultrapure

water. The water vapour production was expressed as the weight loss of water during the experiment, that was determined by weighing the container-template-water system before and after the experiment with a laboratory scale ($\approx 10^{-4}$ g precision). Experiments lasted 2 h and the total amount of evaporated water was in the range of 1 to 2 g.

Author Contributions: Conceptualization, I.F. and J.S.-P.; methodology, I.F., V.J., V.B.B., J.F.-B. and J.S.-P.; software, M.B. and J.S.-P.; validation, I.F. and J.S.-P.; formal analysis, M.B., J.F.-B. and J.S.-P.; investigation, all authors; resources, V.J., J.F.-B., L.F.M., J.S.-P.; data curation, all authors; writing—original draft preparation, I.F. and J.S.-P.; writing—review and editing, all authors; visualization, J.S.-P.; supervision, J.S.-P.; project administration, J.S.-P.; funding acquisition, J.S.-P.

Conflicts of Interest: The authors declare no conflict of interest. The funders had no role in the design of the study; in the collection, analyses, or interpretation of data; in the writing of the manuscript, or in the decision to publish the results.

References

1. Maier, S.A. *Plasmonics: Fundamentals and Applications*; Springer: Berlin/Heidelberg, Germany, 2007.
2. Stockman, M.I.; Kneipp, K.; Bozhevolnyi, S.I.; Saha, S.; Dutta, A.; Ndukaife, J.; Kinsey, N.; Reddy, H.; Guler, U.; Shalaev, V.M.; et al. Roadmap on plasmonics. *J. Opt.* **2018**, *20*, 043001. [CrossRef]
3. Maradudin, A.A.; Sambles, J.R.; Barnes, W.L. *Modern Plasmonics*; Elsevier: Amsterdam, The Netherlands, 2014; Volume 4.
4. West, P.R.; Ishii, S.; Naik, G.V.; Emani, N.K.; Shalaev, V.M.; Boltasseva, A. Searching for better plasmonic materials. *Laser Photonics Rev.* **2010**, *4*, 795–808. [CrossRef]
5. Naik, G.V.; Shalaev, V.M.; Boltasseva, A. Alternative plasmonic materials: Beyond gold and silver. *Adv. Mater.* **2013**, *25*, 3264–3294. [CrossRef] [PubMed]
6. Palik, E. *Handbook of Optical Constants of Solids*; Handbook Series; Academic Press: Cambridge, MA, USA, 1998.
7. Chan, G.H.; Zhao, J.; Hicks, E.M.; Schatz, G.C.; Van Duyne, R.P. Plasmonic properties of copper nanoparticles fabricated by nanosphere lithography. *Nano Lett.* **2007**, *7*, 1947–1952. [CrossRef]
8. Ghodselahi, T.; Vesaghi, M.; Shafiekhani, A.; Baghizadeh, A.; Lameii, M. XPS study of the Cu@ Cu$_2$O core-shell nanoparticles. *Appl. Surf. Sci.* **2008**, *255*, 2730–2734. [CrossRef]
9. Sun, Q.C.; Ding, Y.; Goodman, S.M.; Funke, H.H.; Nagpal, P. Copper plasmonics and catalysis: Role of electron–phonon interactions in dephasing localized surface plasmons. *Nanoscale* **2014**, *6*, 12450–12457. [CrossRef] [PubMed]
10. Kravets, V.; Jalil, R.; Kim, Y.J.; Ansell, D.; Aznakayeva, D.; Thackray, B.; Britnell, L.; Belle, B.; Withers, F.; Radko, I.; et al. Graphene-protected copper and silver plasmonics. *Sci. Rep.* **2014**, *4*, 5517. [CrossRef] [PubMed]
11. Susman, M.D.; Feldman, Y.; Vaskevich, A.; Rubinstein, I. Chemical deposition and stabilization of plasmonic copper nanoparticle films on transparent substrates. *Chem. Mater.* **2012**, *24*, 2501–2508. [CrossRef]
12. Sancho-Parramon, J.; Okorn, B.; Salamon, K.; Janicki, V. Plasmonic resonances in copper island films. *Appl. Surf. Sci.* **2019**, *463*, 847–853. [CrossRef]
13. Peña-Rodríguez, O.; Pal, U. Effects of surface oxidation on the linear optical properties of Cu nanoparticles. *J. Opt. Soc. Am. B* **2011**, *28*, 2735–2739. [CrossRef]
14. Gérard, D.; Gray, S.K. Aluminium plasmonics. *J. Phys. D Appl. Phys.* **2014**, *48*, 184001. [CrossRef]
15. Knight, M.W.; Liu, L.; Wang, Y.; Brown, L.; Mukherjee, S.; King, N.S.; Everitt, H.O.; Nordlander, P.; Halas, N.J. Aluminum plasmonic nanoantennas. *Nano Lett.* **2012**, *12*, 6000–6004. [CrossRef] [PubMed]
16. Knight, M.W.; King, N.S.; Liu, L.; Everitt, H.O.; Nordlander, P.; Halas, N.J. Aluminum for plasmonics. *ACS Nano* **2013**, *8*, 834–840. [CrossRef] [PubMed]
17. Martin, J.; Plain, J. Fabrication of aluminium nanostructures for plasmonics. *J. Phys. D Appl. Phys.* **2014**, *48*, 184002. [CrossRef]
18. Johnson, P.B.; Christy, R.W. Optical constants of the noble metals. *Phys. Rev. B* **1972**, *6*, 4370. [CrossRef]

19. Kreibig, U.; Vollmer, M. *Optical Properties of Metal Clusters*; Springer Science & Business Media: Berlin/Heidelberg, Germany, 2013; Volume 25.

20. Scholl, J.A.; Koh, A.L.; Dionne, J.A. Quantum plasmon resonances of individual metallic nanoparticles. *Nature* **2012**, *483*, 421–427. [CrossRef] [PubMed]

21. Bohren, C.F.; Huffman, D.R. *Absorption and Scattering of Light by Small Particles*; John Wiley & Sons: Hoboken, NJ, USA, 2008.

22. Nicoletti, O.; de La Peña, F.; Leary, R.K.; Holland, D.J.; Ducati, C.; Midgley, P.A. Three-dimensional imaging of localized surface plasmon resonances of metal nanoparticles. *Nature* **2013**, *502*, 80–84. [CrossRef] [PubMed]

23. Zheng, P.; Tang, H.; Liu, B.; Kasani, S.; Huang, L.; Wu, N. Origin of strong and narrow localized surface plasmon resonance of copper nanocubes. *Nano Res.* **2019**, *12*, 63–68. [CrossRef]

24. Kelly, K.L.; Coronado, E.; Zhao, L.L.; Schatz, G.C. The optical properties of metal nanoparticles: The influence of size, shape, and dielectric environment. *J. Phys. Chem. B* **2003**, *1073*, 668–677. [CrossRef]

25. Sönnichsen, C.; Franzl, T.; Wilk, T.v.; von Plessen, G.; Feldmann, J.; Wilson, O.; Mulvaney, P. Drastic reduction of plasmon damping in gold nanorods. *Phys. Rev. Lett.* **2002**, *88*, 077402. [CrossRef]

26. Aizpurua, J.; Bryant, G.W.; Richter, L.J.; De Abajo, F.G.; Kelley, B.K.; Mallouk, T. Optical properties of coupled metallic nanorods for field-enhanced spectroscopy. *Phys. Rev. B* **2005**, *71*, 235420. [CrossRef]

27. Chen, H.; Shao, L.; Li, Q.; Wang, J. Gold nanorods and their plasmonic properties. *Chem. Soc. Rev.* **2013**, *42*, 2679–2724. [CrossRef] [PubMed]

28. Cubukcu, E.; Capasso, F. Optical nanorod antennas as dispersive one-dimensional Fabry–Pérot resonators for surface plasmons. *Appl. Phys. Lett.* **2009**, *95*, 201101. [CrossRef]

29. Dorfmuller, J.; Vogelgesang, R.; Weitz, R.T.; Rockstuhl, C.; Etrich, C.; Pertsch, T.; Lederer, F.; Kern, K. Fabry-Perot resonances in one-dimensional plasmonic nanostructures. *Nano Lett.* **2009**, *9*, 2372–2377. [CrossRef] [PubMed]

30. Novotny, L. Effective wavelength scaling for optical antennas. *Phys. Rev. Lett.* **2007**, *98*, 266802. [CrossRef] [PubMed]

31. Nordlander, P.; Oubre, C.; Prodan, E.; Li, K.; Stockman, M. Plasmon hybridization in nanoparticle dimers. *Nano Lett.* **2004**, *4*, 899–903. [CrossRef]

32. Grillet, N.; Manchon, D.; Bertorelle, F.; Bonnet, C.; Broyer, M.; Cottancin, E.; Lermé, J.; Hillenkamp, M.; Pellarin, M. Plasmon coupling in silver nanocube dimers: Resonance splitting induced by edge rounding. *ACS Nano* **2011**, *5*, 9450–9462. [CrossRef]

33. Sancho-Parramon, J.; Janicki, V.; Zorc, H. On the dielectric function tuning of random metal-dielectric nanocomposites for metamaterial applications. *Opt. Express* **2010**, *18*, 26915–26928. [CrossRef]

34. Lončarić, M.; Sancho-Parramon, J.; Zorc, H. Optical properties of gold island films—A spectroscopic ellipsometry study. *Thin Solid Films* **2011**, *519*, 2946–2950. [CrossRef]

35. Stenzel, O. *Optical Coatings: Material Aspects in Theory and Practice*; Springer Science & Business: Berlin/Heidelberg, Germany, 2014; Volume 54.

36. Singer, R.; Leitner, A.; Aussenegg, F. Structure analysis and models for optical constants of discontinuous metallic silver films. *JOSA B* **1995**, *12*, 220–228. [CrossRef]

37. Stenzel, O.; Macleod, A. Metal-dielectric composite optical coatings: Underlying physics, main models, characterization, design and application aspects. *Adv. Opt. Technol.* **2012**, *1*, 463–481. [CrossRef]

38. Sancho-Parramon, J.; Janicki, V.; Zorc, H. Tuning the effective dielectric function of thin film metal-dielectric composites by controlling the deposition temperature. *J. Nanophotonics* **2011**, *5*, 051805. [CrossRef]

39. Martin, J.; Proust, J.; Gérard, D.; Plain, J. Localized surface plasmon resonances in the ultraviolet from large scale nanostructured aluminum films. *Opt. Mater. Express* **2013**, *3*, 954–959. [CrossRef]

40. Lebedev, A.; Stenzel, O.; Quinten, M.; Stendal, A.; Röder, M.; Schreiber, M.; Zahn, D. A statistical approach for interpreting the optical spectra of metal island films: Effects of multiple scattering in a statistical assembly of spheres. *J. Opt. A Pure Appl. Opt.* **1999**, *1*, 573. [CrossRef]

41. Held, M.; Stenzel, O.; Wilbrandt, S.; Kaiser, N.; Tünnermann, A. Manufacture and characterization of optical coatings with incorporated copper island films. *Appl. Opt.* **2012**, *51*, 4436–4447. [CrossRef] [PubMed]

42. Dalacu, D.; Martinu, L. Optical properties of discontinuous gold films: Finite-size effects. *JOSA B* **2001**, *18*, 85–92. [CrossRef]

43. Neumann, O.; Urban, A.S.; Day, J.; Lal, S.; Nordlander, P.; Halas, N.J. Solar vapor generation enabled by nanoparticles. *ACS Nano* **2012**, *7*, 42–49. [CrossRef]

44. Bae, K.; Kang, G.; Cho, S.K.; Park, W.; Kim, K.; Padilla, W.J. Flexible thin-film black gold membranes with ultrabroadband plasmonic nanofocusing for efficient solar vapour generation. *Nat. Commun.* **2015**, *6*, 10103. [CrossRef]

45. Zhou, L.; Tan, Y.; Ji, D.; Zhu, B.; Zhang, P.; Xu, J.; Gan, Q.; Yu, Z.; Zhu, J. Self-assembly of highly efficient, broadband plasmonic absorbers for solar steam generation. *Sci. Adv.* **2016**, *2*, e1501227. [CrossRef]

46. Baffou, G.; Quidant, R.; García de Abajo, F.J. Nanoscale control of optical heating in complex plasmonic systems. *ACS Nano* **2010**, *4*, 709–716. [CrossRef]

47. Gérardy, J.; Ausloos, M. Absorption spectrum of clusters of spheres from the general solution of Maxwell's equations. II. Optical properties of aggregated metal spheres. *Phys. Rev. B* **1982**, *25*, 4204. [CrossRef]

48. Myroshnychenko, V.; Rodríguez-Fernández, J.; Pastoriza-Santos, I.; Funston, A.M.; Novo, C.; Mulvaney, P.; Liz-Marzan, L.M.; de Abajo, F.J.G. Modelling the optical response of gold nanoparticles. *Chem. Soc. Rev.* **2008**, *37*, 1792–1805. [CrossRef] [PubMed]

49. De Abajo, F.G.; Howie, A. Retarded field calculation of electron energy loss in inhomogeneous dielectrics. *Phys. Rev. B* **2002**, *65*, 115418. [CrossRef]

50. Hohenester, U.; Trügler, A. MNPBEM–A Matlab toolbox for the simulation of plasmonic nanoparticles. *Comput. Phys. Commun.* **2012**, *183*, 370–381. [CrossRef]

51. Lee, W.; Park, S.J. Porous anodic aluminum oxide: Anodization and templated synthesis of functional nanostructures. *Chem. Rev.* **2014**, *114*, 7487–7556. [CrossRef] [PubMed]

52. Vojkuvka, L.; Santos, A.; Pallarès, J.; Ferré-Borrull, J.; Marsal, L.F.; Celis, J.P. On the mechanical properties of nanoporous anodized alumina by nanoindentation and sliding tests. *Surf. Coat. Technol.* **2012**, *206*, 2115–2124. [CrossRef]